1-1-2018

Enhanced thermoelectric performance through synergy of resonance levels and valence band convergence via Q/In (Q = Mg, Ag, Bi) co-doping

Lijuan Zhang
University of Wollongong, lz813@uowmail.edu.au

Peng Qin
Kunming University of Science and Technology

Chao Han
University of Wollongong, chan@uow.edu.au

Jian Li Wang
University of Wollongong, jianli@uow.edu.au

Zhenhua Ge
Kunming University of Science and Technology

See next page for additional authors

Enhanced thermoelectric performance through synergy of resonance levels and valence band convergence via Q/In (Q = Mg, Ag, Bi) co-doping

Abstract

The temperature-dependent evolution of heavy-hole valence band contribution to the Seebeck coefficients of SnTe-based thermoelectric materials is revealed in situ by neutron and synchrotron powder diffraction. The additional carriers with high effective mass are created in a heavy-hole valence band above 493 K, which contribute to the electrical transport, and lead to a significant enhancement of the Seebeck coefficient at high temperature. In addition, remarkably improved electrical transport properties are achieved through the synergetic effects of the resonance levels, the valence band convergence, and the carrier concentration optimization by co-doping with Mg & In, Ag & In and Bi & In. Significant reduction in the lattice thermal conductivity is obtained by multiscale phonon scattering over a wide spectrum via atomic point defects, nanoscale elongated screw dislocations with random directions, and the microscale grain boundaries caused by sintering. As a result, a high figure of merit, ZT, of ~1 at 873 K is obtained for the Mg0.015In0.015Sn0.97Te sample.

Disciplines

Engineering | Physical Sciences and Mathematics

Publication Details

Zhang, L., Qin, P., Han, C., Wang, J., Ge, Z., Sun, Q., Cheng, Z., Li, Z. & Dou, S. Xue. (2018). Enhanced thermoelectric performance through synergy of resonance levels and valence band convergence via Q/In (Q = Mg, Ag, Bi) co-doping. Journal of Materials Chemistry A, 6 (6), 2507-2516.

Authors

Lijuan Zhang, Peng Qin, Chao Han, Jian Li Wang, Zhenhua Ge, Qiao Sun, Zhenxiang Cheng, Zhen Li, and Shi Xue Dou

Journal Name

ARTICLE

Enhanced Thermoelectric Performance through Synergy of Resonance Levels and Valence Band Convergence via Q/In (Q = Mg, Ag, Bi) Co-Doping

Received 00th January 20xx,
Accepted 00th January 20xx

DOI: 10.1039/x0xx00000x

www.rsc.org/

Li Juan Zhang[a], Peng Qin[c], Chao Han[a], Jian Li Wang[a], Zhen Hua Ge[c], Qiao Sun[b], Zhen Xiang Cheng[a], Zhen Li, [a, b,]* and Shi Xue Dou[a]

The temperature-dependent evolution of heavy-hole valence band contribution to the Seebeck coefficients of SnTe-based thermoelectric materials is revealed *in situ* by neutron and synchrotron powder diffraction. The additional carriers with high effective mass are created in heavy-hole valence band above 493 K, which contribute to the electrical transport, and lead to a significant enhancement of the Seebeck coefficient at high temperature. In addition, remarkably improved electrical transport properties are achieved through the synergetic effects of the resonance levels, the valence band convergence, and the carrier concentration optimization by co-doping with Mg&In, Ag&In and Bi&In. The significant reduction in the lattice thermal conductivity is obtained by multiscale phonon scattering over a wide spectrum via atomic point defects, nanoscale elongated screw dislocations with random directions, and the microscale grain boundaries caused by the sintering. As a result, a high figure of merit, *ZT*, of ~1 at 873 K is obtained for the $Mg_{0.015}In_{0.015}Sn_{0.97}Te$ sample.

Introduction

Thermoelectric technology has received considerable interests, as it can directly convert waste heat into electricity in the absence of any moving parts or liquid media, which could significantly reduce energy consumption and carbon emissions.[1-5] Thermoelectric materials are the building blocks of this technology, and their performance is characterized by the dimensionless figure of merit (*ZT*), defined as $ZT = \alpha^2\sigma T/(\kappa_{lat} + \kappa_{ele})$, where α is the Seebeck coefficient, σ is the electrical conductivity, κ_{lat} is the lattice thermal conductivity, κ_{ele} is the electronic thermal conductivity, and T is absolute temperature.[6] Metal chalcogenides such as bismuth and lead chalcogenides have been well investigated, among which, lead chalcogenides and their alloys (PbX, X = S, Se, and Te) have been engineered to achieve record *ZT* through band engineering (resonant levels, band convergence/band alignment),[7-10] and hierarchical all-scale phonon scattering (atomic scale point defects, nanoscale precipitates, and microscale grain boundaries).[10-15] These strategies have recently been applied to tin chalcogenides,[16-21] which are new potential environmentally friendly thermoelectric materials with the same level performance as PbTe.

Similar to PbTe and PbSe, tin telluride (SnTe) has two valence bands. One is defined as the light-hole valence band at the L point of the highly symmetric Brillouin zone, and the other one is called the heavy-hole valence band and lies at the Σ point energetically below the L point. In contrast to the small band gap (~ 0.18 eV, 300 K), its energy separation between these two valence bands is nearly twice as great, around ~ 0.3 eV at 300 K,[22] which prevents significant contribution of the Σ band to the Seebeck coefficient for SnTe. In addition, the very small band gap of SnTe is not favourable for retaining high thermoelectric performance at high temperatures because of bipolar diffusion. Another concern is the ultra-high hole density (>10^{21} cm^{-3}) caused by the very large number of intrinsic Sn lattice vacancies.[23, 24] Recent studies, however, have significantly demonstrated that SnTe could be a promising thermoelectric material through the introduction of resonant levels (In dopant),[16, 17, 21, 25] valence band convergence (Cd,[17, 20] Mg,[19] Hg,[26] Ag,[25, 27] and Mn[18] dopants), and optimization of the carrier concentration (Bi, Sb, and Ga dopants).[26, 28, 29] Zhang et al.[21] reported that In is an effective dopant for creating resonance levels around the Fermi level inside the valence band. With the benefit of valence band convergence via Mg doping, a high *ZT* of 1.2 has been achieved at 860 K.[19] It is important to note that the formation of a resonance state in the valence band significantly enhances the Seebeck coefficient of SnTe at low temperature.[7, 9] In addition, the convergence of the valence band widens the band gap and

[a] Institute for Superconducting and Electronic Materials, University of Wollongong, Squires Way, North Wollongong, New South Wales 2500, Australia. * Email: zhenli@suda.edu.cn; zhenl@uow.edu.au
[b] School of Radiation Medicine and Radiation Protection, Collaborative Innovation Center of Radiation Medicine of Jiangsu Higher Education Institutions, Soochow University, 199 Ren Ai Road, Suzhou Industrial Park, Suzhou 215123, China.
[c] Faculty of Materials Science and Technology, Kunming University of Science and Technology, 68 Wenchang Road, Kunming 650093, China.

Electronic Supplementary Information (ESI) available: XRD, Densities, temperature dependent diffusivity (D), heat capacity (C_p), Lorenz number (L), electronic thermal conductivity of $Mg_{x/2}In_{x/2}Sn_{1-x}Te$, $Ag_{x/2}In_{x/2}Sn_{1-x}Te$, and $Bi_{x/2}In_{x/2}Sn_{1-x}Te$, and STEM/STEM EDS of $Mg_{0.015}In_{0.015}Sn_{0.97}Te$. See DOI: 10.1039/x0xx00000x

lowers the energy separation, which improves the Seebeck coefficient at high temperature by improving the electronic density of states and inhibiting bipolar conduction.[20] Thus, it is a significant advance to introduce the synergetic effects of resonance levels and valence band convergence to improve the Seebeck coefficient and thermoelectric performance over a broad temperature range. Moreover, it has been demonstrated that as the temperature increases, the L valence band of PbTe shifts down, while the energy position of the Σ band roughly stays constant, which leads to an effective band convergence at some temperature point (*i.e.*, >800 K), as shown in Figure 1a.[21] The evolution of Σ band as temperature increases, however, and its relationship to the contribution of electrical transport and Seebeck coefficient have not been fully investigated and understood.

In this work, neutron and synchrotron powder diffraction measurements were applied to pristine SnTe to reveal its temperature-dependent Σ band contribution to its Seebeck coefficient, which indicates that additional carriers with high effective mass were generated in heavy-hole valence band above 493 K. These "heavy" carriers contributed to the electrical transport, and played a significant role in the enhancement of the Seebeck efficient at high temperature (> 493 K). Moreover, the coexistence of resonant levels, band convergence, and/or the carrier concentration optimization induced by Mg&In, Ag&In and Bi&In co-doping has synergistically contributed to a large improvement in the Seebeck coefficients of SnTe-based materials over a wide temperature range from 323 to 873 K. In addition, the atomic scale point defects, the nanoscale elongated screw dislocations with random directions, and the microscale grain boundaries caused by the sintering efficiently scatter a wide spectrum of heat-carrying phonons, leading to a remarkable reduction in the lattice thermal conductivity. With the benefit of these factors, a high *ZT* of ~1 at 873 K was obtained for $Mg_{0.015}In_{0.015}Sn_{0.97}Te$ sample, being 80% higher than that of pristine SnTe. The average *ZT* in the range of 323 to 873 K is considerably improved 2.6 times, *i.e.*, from ~0.14 for pristine SnTe to ~0.51 for $Mg_{0.015}In_{0.015}Sn_{0.97}Te$.

Experimental and theoretical section

Sample preparation

High-purity Sn (Sigma Aldrich, 99.8%), Te (Alfa Aesar, 99.999+%), In (Sigma Aldrich, 99.99%), Mg (Sigma Aldrich, 99+%), Ag (Sigma Aldrich, 99.9+%), and Bi (Alfa Aesar, 99.99+%) were weighted and mixed according to the nominal formula of $Q_{x/2}In_{x/2}Sn_{1-x}Te$ (Q = Mg, Ag, and Bi; x = 0, 0.01, 0.02, 0.03, and 0.04), and put inside 15-mm-diameter quartz tubes in an argon filled glove box. The tubes were flame-sealed under vacuum and then placed in larger 26-mm-diameter quartz tubes, which were evacuated and flame-sealed again. The outer tube was used to protect the crystals from oxidation by air, because the inner tube could break due to the considerable difference in thermal expansion between the crystals and quartz. The double sealed quartz was slowly heated to 1273 K in 10 h, held at this temperature for 8 h, and then cooled to room temperature by turning off the furnace power. In a typical experiment, 2.2504 g Te, 2.0308 g Sn, 0.0064 g Mg and 0.0304 g In were used to prepare ~ 4.318 g ingots of $Mg_{0.015}In_{0.015}Sn_{0.97}Te$ sample. The resultant ingots were ground into fine powders and then sintered by the spark plasma sintering (SPS) method at 773 K for 5 min in a 20 mm-diameter graphite die under an axial compressive stress of 50 MPa under the vacuum.

Characterization

Scanning/transmission electron microscopy (S/TEM) S/TEM and energy dispersive spectroscopy (EDS) were carried out in a JEOL JEM-ARM 200F microscope operated at 200 kV. The thin TEM specimen was prepared by focused ion beam (FIB) at a moderate voltage (16 keV), which was then followed by cleaning at a lower voltage (5 keV) to remove contaminants.

Powder X-ray diffraction (PXRD) Samples ground with an agate mortar were used for PXRD characterization. The powder diffraction patterns were obtained with Cu Kα (λ = 1.5418 Å) radiation in a reflection geometry on an Inel diffractometer operating at 40 kV and 25 mA, and equipped with a position-sensitive detector.

Neutron powder diffraction (NPD) 3.5 g of SnTe powder was packed in a cylindrical alumina holder with a diameter of 8 mm, and used for neutron powder diffraction measurements. The NPD patterns were collected on the high-resolution powder diffractometer ECHIDNA (Australian Nuclear Science and Technology Organization) with a wavelength of 1.6215 Å. The powder sample was heated from 300 to 700 K under vacuum on a cylindrical computer controlled furnace. The collecting time for one pattern was around 2 h over a wide 2-thetra range from 6.5˚ to 164˚. Rietveld refinements of the structure were carried out using the FULLPROF program package.

Synchrotron powder diffraction (SPD) 4 mg of ground SnTe powder was packed in cylindrical quartz capillary tubes with a diameter of ~0.3 mm, and used for Synchrotron powder diffraction measurements. The SPD patterns were collected on the Powder Diffraction beamline at the Australian Synchrotron. Two wavelengths (λ = 0.59002 Å and 0.6885 Å) were used for the synchrotron powder diffraction experiments. The short wavelength was used for pristine SnTe, and the longer one was selected for Mg&In, and Ag&In co-doped samples. The powders were heated under argon atmosphere from room temperature to 873 K. The collecting time for one pattern was around 10 min over a wide 2-thetra range from 3˚ to 83˚.

Hall measurement The measurement of room-temperature Hall coefficient was carried out on a Physical Properties Measurements System (Quantum Design PPMS-9) by using the four-contact Hall-bar geometry. The carrier mobility (μ) and carrier concentration (N_p) were estimated from the formulas: $\mu = \sigma R_H$ and $Np = 1/(eR_H)$, where σ is the electrical conductivity, R_H is the Hall coefficient for holes, and e is the carrier charge.

Electrical Property The electrical conductivity and the Seebeck coefficient were measured simultaneously on an Ozawa RZ2001i (Japan) instrument under argon atmosphere from 323 to 873 K. Bars with dimensions of ~6 × 2 × 2 mm^3 were cut from pellets

sintered by SPS and used for measurements. The samples were coated with a thin (~0.1 - 0.2 mm) layer of boron nitride to protect the instrument.

Thermal Conductivity The thermal conductivity was calculated from $\kappa = DC_pd$, where D is the thermal diffusivity coefficient, C_p is the specific heat capacity, and d is the density.[30] Disks with dimensions of Ø (6-10) × 1 mm^3 were cut from pellets and used for the thermal diffusivity coefficient measurement on the LFA457 instrument (Germany) (Figure S8). The samples were coated with a thin layer of graphite to minimize errors from the emissivity of the material. The C_p values were indirectly derived from a representative sample (DSC 204) over the range from 323 to 573 K, and then simulated to 873 K based on the Debye model (Figure S9). The d values were measured according to the Archimedes method. Highly dense (>95% of theoretical density) of pellets were obtained (Table S1). The total thermal conductivity is composed of the electronic thermal conductivity (κ_{ele}) and the lattice thermal conductivity (κ_{lat}). The electron contribution is assessed by the Wiedemann-Franz law, $\kappa_{ele} = L\sigma T$, where L is Lorenz number, σ is electrical conductivity, and T is absolute temperature.[17] In our work, L is evaluated from the formula $L = 1.5 + \exp[-|\alpha|/116]$, where L and α are in 10^{-8} W Ω K^{-2} and in μV K^{-1}, respectively (see the Supporting information Figure S7).[31]

Results and discussion

Temperature dependence of Σ band contribution to the Seebeck coefficient

As demonstrated previously, the Σ valence band contributes additional carriers to electrical transport at elevated temperature, leading to a significant enhancement of the Seebeck coefficient, as shown in Figure 1a.[1, 32] In order to fully understand the temperature-dependent evolution of Σ band contribution to electrical transport and its relationship to the Seebeck coefficient, the *in situ* neutron and synchrotron powder diffraction measurements were carried out for pristine SnTe over a wide temperature range.

The neutron powder diffraction (PND) patterns were collected from 300 to 700 K (Figure 1b), and the corresponding unit cell volumes as a function of temperature are shown in Figure 1c. It can be seen that the unit cell volume grows larger as the temperature increases; however, the enlargement is diminished above 493 K. Specifically, the room-temperature unit cell volume is 251.31 Å^3, it quickly increases to 254.10 Å^3 at 483 K, and then slowly rises to 254.78 Å^3 as the temperature increases to 700 K. This crossover temperature is also confirmed by the derivative of the unit cell volume with respect to the temperature, as shown in the inset (Figure 1c). According to the Dulong-Petit law plot based on the thermal expansion, the deviation of the unit cell volume could be ascribed to the intrinsic structural transformation of SnTe, which can be also confirmed by the endothermic peak of DSC analysis around 507 K (Figure S4). It is interesting to note that this discrepancy has also been observed in T-dependent Hall coefficients measurement.[20] A similar crossover peak, around 523 K, was observed in the R_H-T plot, which is ascribed to the presence of the heavy-hole valence band on the contribution of the electrical transport. Thus, one of the possible mechanisms for this deviation of the unit cell volume based on thermal expansion is the onset of the Σ band to electrical transport, indicating the potential existence of valence bands convergence at elevated temperature.[1, 32] In addition, the *in situ* synchrotron powder diffraction (SPD) patterns are collected over a wide temperature range from 303 to 873 K as shown in Figure 1d. As expected, the synchrotron diffraction presents higher resolution and it is able to distinguish the peak shifting of SnTe comparing to the neutron powder diffraction. For example, the peak of (200), which is located at the 2-theta of ~10.71° at 303 K, gradually shifts to smaller angles ~10.69°, 10.67°, 10.64°, 10.61° and 10.58° when the temperature increases from 303 K to 373, 523, 673, 773, and 873 K due to the thermal expansion (Figure 1e), which is difficult to be separated from the neutron diffraction patterns. It is interesting to note that the relative intensity of the peak of (200) presents a double increase above 523 K. Such abnormal intensity increase is observed in all the other peaks above 523 K. The peak intensity is kept when the samples are cooled from 523 K to the room temperature (Figures S5-S6), which indicates that SnTe powders undergo an irreversible grain recrystallization and growth above 523 K. The abnormal intensity increase is ascribed to the introduction of strains during the preparation of SPD powders. The strain is released as the temperature increases, which promotes the grain growth (Figure S4).

According to the Mott formula, the Seebeck coefficient can be defined by Equation (1):[33]

$$\alpha = \frac{8\pi^2\kappa_B^2}{3\,e\hbar^2} m_d^* T \left(\frac{\pi}{3n}\right)^{\frac{2}{3}} \quad (1)$$

where k_B, e, $\hbar$, m_d^* are the Boltzmann constant, carrier charge, Plank constant, and total DOS effective mass respectively. For a given carrier concentration, the Seebeck coefficient can be estimated by total DOS effective mass, m_d^*, which can be defined in Equation (2):[3, 34]

$$m_d^* = N_V^{\frac{2}{3}} m_b^* \quad (2)$$

where N_V is the number of degenerate carrier pockets and m_b^* is the average DOS effective mass for each pocket (single-band DOS effective mass). When the Σ valence band attends to electrical transport, the Seebeck coefficient will be enhanced due to the dramatically higher effective mass of carriers in the Σ valence band by a factor of $N_V^{\frac{2}{3}}$, where N_V is 4 for the L band and increases to 12 for the Σ band.[34]

Figure 2 presents the Seebeck coefficient as a function of temperature for pristine SnTe. The α values slowly increase from ~17 μV K^{-1} at room temperature to ~27 μV K^{-1} at 473 K, and then drastically increase to ~127 μV K^{-1} as the temperature increases to 873 K.

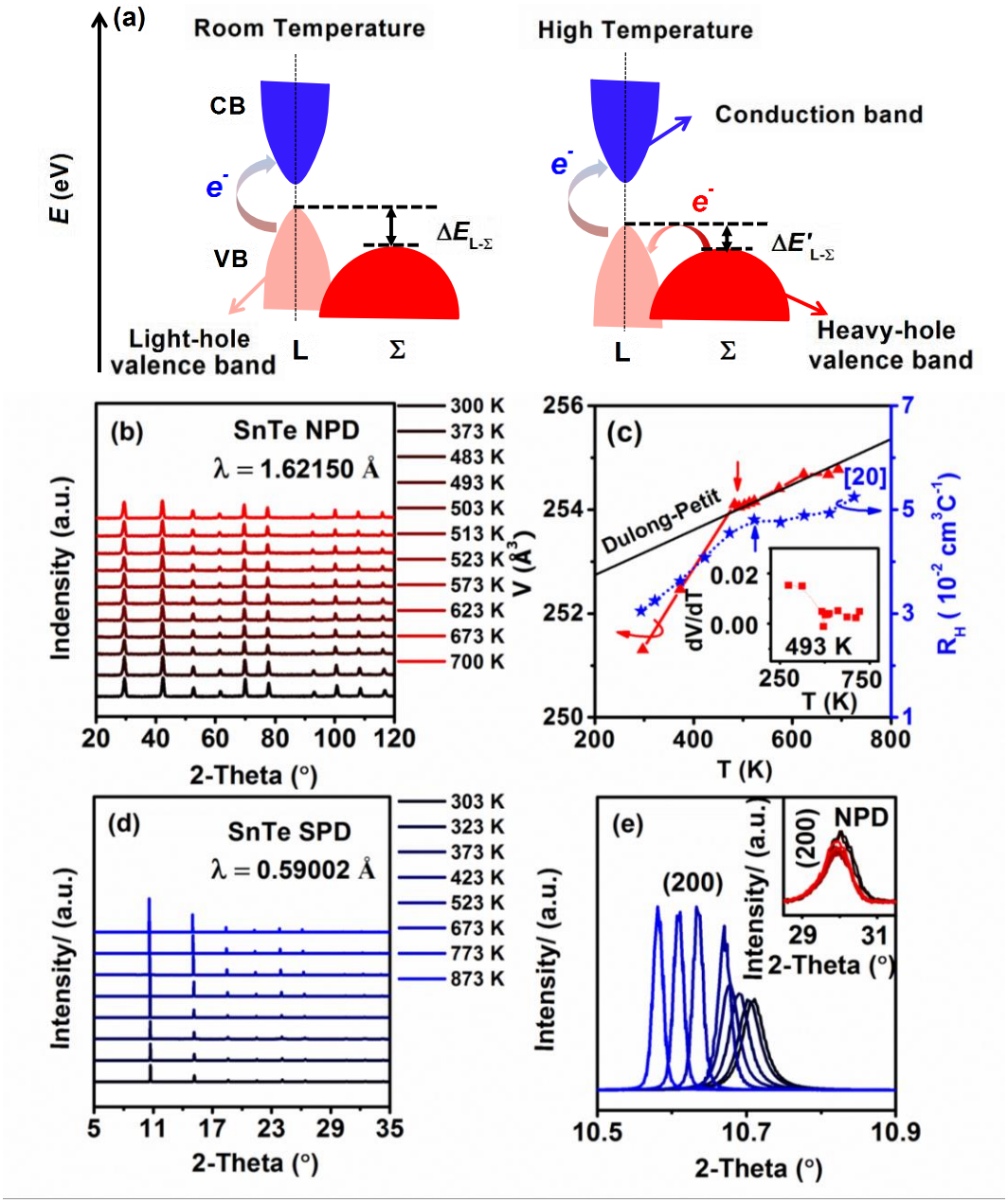

Figure 1. (a) Schematic diagram of the carriers transport of SnTe at room temperature and high temperature among the conduction band (CB), light-hole valence band (VBL), and heavy-hole valence band (VBΣ); (b) Neutron powder diffraction patterns for pristine SnTe at 300 - 700 K; (c) Corresponding Rietveld refined unit cell volume (V) as a function of temperature as it is increased in (b). Inset is the derivative of the unit cell volume with respect to temperature, presenting a turndown point at 493 K. The red line is the theoretical unit cell volume according to the Dulong-Petit law; values from previous reports of the temperature-dependent Hall coefficient are also presented;[20] (d) Synchrotron powder diffraction patterns for pristine SnTe at 303 - 873 K; (e) Enlarged patterns in the 2-theta range of 10.5˚ - 10.8˚ for peak (200) in (d). Inset is corresponding NPD enlarged patterns for peak of (200) in (b).

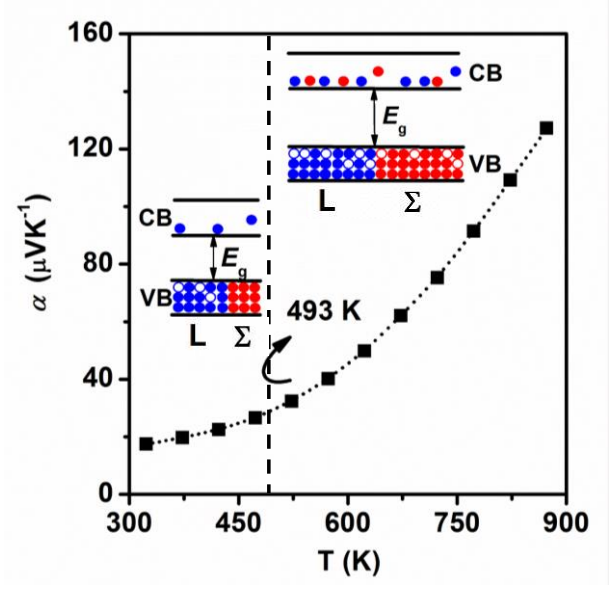

Figure 2. Seebeck coefficient as a function of temperature for pristine SnTe. Left inset is a schematic illustration of the distribution of holes at low temperature, which indicates that the holes are mainly located in the L valence band; right inset is a schematic illustration of the distribution of holes at high temperature, indicating that additional holes are generated from the Σ valence band as the temperature increases above 493 K.

This increased enhancement of the Seebeck coefficient is mainly ascribed to the attendance of the higher effective mass of carriers to the electrical transport at elevated temperature (Figure 1). The inset is a schematic illustration of the distribution of carriers as the temperature increases. Additional carriers with higher effective mass are generated in Σ band arising from the thermal excitation of holes from the L to Σ valence band above 493 K.

Synergy of resonance levels, valence band convergence and carrier concentration via Mg&In, Ag&In and Bi&In co-doping

Besides the temperature dependence of Σ band contribution to Seebeck coefficient, the L and Σ valence bands can be further converged by properly doping due to the lowered Fermi level. In this part, the band structure of SnTe was engineered by co-doping with Mg&In, Ag&In and Bi&In, which leads to a notable enhancement of the thermoelectric performance over a wide temperature range. All three-types of doped samples are characterized as single cubic SnTe with the *Fm-3m* space group, as shown in PXRD patterns in the Supporting Information Figures S1-S3. The Seebeck coefficient as a function of temperature for $Mg_{x/2}In_{x/2}Sn_{1-x}Te$, $Ag_{x/2}In_{x/2}Sn_{1-x}Te$, and $Bi_{x/2}In_{x/2}Sn_{1-x}Te$ are presented in Figure 3a-c, respectively. It can be seen that the α values of Mg&In and Ag&In co-doped samples are strongly dependent on the dopant concentration, and the room-temperature values are notably improved 2 - 4 times in comparison with that of pristine SnTe. This significant improvement of room-temperature Seebeck coefficents is mainly attributed to the introduction of resonant levels in the valence band *via* In doping.[17, 21] This resonant levels, which are also observed in Tl doped PbTe and Sn doped Bi_2Te_3 samples,[7, 9, 35] can improve the Seebeck coefficient through two mechanisms, *i.e.,* (1) electrons in extended states (plane-wave-like wavefunction created by In impurities) can carry electricity and heat, and contribute to the Seebeck coefficient in a nearly temperature-independent way; and (2) resonant scattering presents a strong electron energy filtering effect, and increase the Seebeck coefficient at low temperature where the electron-phonon interactions are weaker.[9] In addition, the α values present a significant improvement over a wide temperature range from 323 to 873 K, which provides an evidence of the narrowed energy separation at low temperature through Mg and Ag doping.[19, 25, 27] In contrast to the cases of Mg&In and Ag&In co-doping, the α values are dramatically increased for Bi&In co-doped samples when compared with pristine SnTe at high temperature (Figure 3c).

To shed more light on the doping effects of the different combined dopants (Mg&In, Ag&In and Bi&In) on the Seebeck coefficients, we selected the samples with 3% doping concentration for comparison in Figure 3d, since the thermoelectric properties were optimized and achieved their maximum values at 3 mol % doping fraction. It can be seen that the enhancement of Seebeck coefficients for $Mg_{0.015}In_{0.015}Sn_{0.97}Te$ and $Ag_{0.015}In_{0.015}Sn_{0.97}Te$ are similar over a broad temperature range due to the same introduction of resonant levels in the valence band *via* In doping, [16, 17, 21, 25] and the similar convergence of the valence band *via* Mg and Ag doping,[19, 25, 27] as mentioned above. The improvement, however, in the case of $Bi_{0.015}In_{0.015}Sn_{0.97}Te$, is better identified above 473 K due to the pronounced reduction of the carrier concentration by Bi doping, [26, 28] which will be discussed later. Specifically, at 323 K, the Seebeck coefficients of pristine SnTe, $Mg_{0.015}In_{0.015}Sn_{0.97}Te$, $Ag_{0.015}In_{0.015}Sn_{0.97}Te$, and $Bi_{0.015}In_{0.015}Sn_{0.97}Te$ are ~17, 76, 74, and 66 μV K^{-1}, and they increase to ~127, 147, 137, and 160 μV K^{-1} at 873 K, respectively.

As mentioned above, for pristine SnTe the intrinsic *T*-dependent contribution of Σ valence band to the electrical transport above 493 K is observed. This behaviour still exists after chemical doping. The Rietveld refined unit cell volumes of doped samples from their SPD patterns (Figures S5 and S6) as a function of temperature are shown as inset in Figure 3d. It can be seen that the unit cell volumes of doped samples exhibits the similar crossover temperature (~493 K) with a slight curvature comparing with that of pristine SnTe, which provides the evidence of the presence of intrinsic structural transformation related to the onset of Σ valence band to electrical transport. It is important to note that, although the intrinsic *T*-dependent contribution of Σ valence band to the electrical transport presents degeneration after chemical doping, the Seebeck coefficient of co-doped SnTe shows the improvement over a broad temperature range because of the synergy of resonance levels,[16, 17, 21, 25] valence band convergence[19, 25, 27] and carrier concentration[26, 28] via Mg&In, Ag&In and Bi&In co-doping (Figure 3a-c).

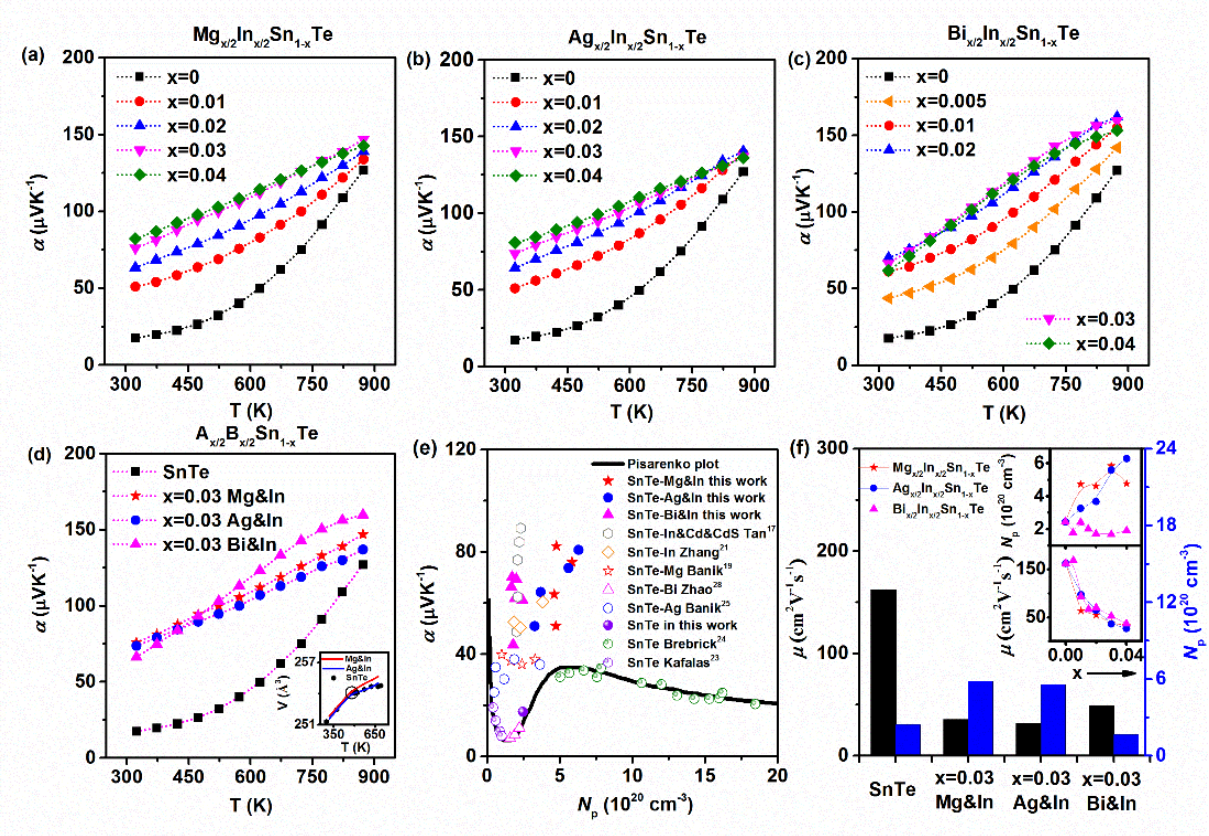

Figure 3. Seebeck coefficient as a function of temperature for (a) $Mg_{x/2}In_{x/2}Sn_{1-x}Te$; (b) $Ag_{x/2}In_{x/2}Sn_{1-x}Te$; (c) $Bi_{x/2}In_{x/2}Sn_{1-x}Te$. (d) Comparison of temperature-dependent Seebeck coefficient for pristine and doped samples with 3% doping concentration. The inset of Figure (d) is the Rietveld refined unit cell volume as a function of temperature from SPD (Mg&In and Ag&In co-doped SnTe, λ= 0.6885 Å) and NPD (pristine SnTe, λ= 1.62150 Å). (e) Room-temperature Pisarenko plot for $Mg_{x/2}In_{x/2}Sn_{1-x}Te$, $Ag_{x/2}In_{x/2}Sn_{1-x}Te$, and $Bi_{x/2}In_{x/2}Sn_{1-x}Te$ samples in comparison with reported data on In-doped,[21] Mg-doped,[19] Ag-doped,[25] Bi-doped,[28] undoped,[23, 24] and In&Cd&CdS-alloyed[17] SnTe. The solid line is based on the single valence band (VBM) model.[21] (f) Carrier concentration and carrier mobility for pristine and doped samples with 3% doping concentration. The top inset is carrier concentration as a function of doping concentration for $Mg_{x/2}In_{x/2}Sn_{1-x}Te$, $Ag_{x/2}In_{x/25}n_{1-x}Te$, and $Bi_{x/2}In_{x/2}Sn_{1-x}Te$ samples. The bottom inset is carrier mobility as a function of doping concentration for these samples.

To further understand the change in the Seebeck coefficient due to three-types of dopants, it is significant to compare the room temperature α versus N_p plots for $Mg_{x/2}In_{x/2}Sn_{1-x}Te$, $Ag_{x/2}In_{x/2}Sn_{1-x}Te$ and $Bi_{x/2}In_{x/2}Sn_{1-x}Te$ with the well-established Pisarenko plot obtained from a single valence band model (VBM).[21] As shown in Figure 3e, the plots of pristine SnTe in this work, together with those of previously reported Bi-doped[28] and undoped[23, 24] SnTe exactly follow the Pisarenko plot. The Seebeck coefficients of the Mg&In, Ag&In, and Bi&In co-doped SnTe in this work are much higher than the theoretical prediction, however, which is similar to the results for Mg-,[19] Ag-,[25] and In-doped[21] SnTe, but presents higher enhancement of the Seebeck coefficients than those of the individual doping cases. These higher enhancements are ascribed to the synergistic effects arising from (i) the resonant level introduced by In-dopant, (ii) the valence band convergence induced by Mg and Ag dopants, and/or (iii) the carrier concentration optimization by Mg-, Ag-, and Bi-doping.

The room temperature carrier concentration for the three-types of dopants with 3% doping concentration is shown in Figure 3f. At the identical doping fraction, the introduction of Mg&In and Ag&In co-dopants increases the carrier concentration from the 2.45 × 10^{20} cm^{-3} for pristine SnTe to 5.85 × 10^{20} and 5.60 × 10^{20} cm^{-3} for Mg&In and Ag&In, respectively, but the introduction of Bi&In co-dopants leads to the reduction in N_p value to around 1.67 × 10^{20} cm^{-3}. The corresponding doping concentration-dependent carrier concentrations for $Mg_{x/2}In_{x/2}Sn_{1-x}Te$, $Ag_{x/2}In_{x/2}Sn_{1-x}Te$, and $Bi_{x/2}In_{x/2}Sn_{1-x}Te$ are presented in the top inset. It is well known that pristine SnTe has a high hole concentration of ~1.8 × 10^{20} cm^{-3} at room temperature because of the presence of intrinsic Sn vacancies.[20, 21, 28] In the case of the Mg&In and Ag&In co-doped samples, their room-temperature N_p roughly increases with increasing doping concentration, which is consistent with expectation of the electron acceptor roles of In,[21] Mg,[19] and Ag[25] dopants in SnTe (Figure 3f). In contrast, the carrier concentrations of Bi&In co-doped samples show a significant reduction at all doping concentrations, which is attributed to the nature of the electron donor role of Bi dopant in SnTe.[28] It should be noted that the effects of the different types of dopants on the carrier concentration of SnTe are not very clear as yet. The room temperature carrier mobility (μ) of three-types of dopants in Figure 3f shows a significant reduction, *i.e.*, from 162.75 cm^2 V^{-1} s^{-1} for pristine SnTe to 38.33, 36.50, and 52.54 cm^2 V^{-1} s^{-1} for Mg&In Ag&In, and Bi&In doped SnTe, respectively. The bottom inset in Figure 3f shows the room

temperature carrier mobility as a function of doping concentration for $Mg_{x/2}In_{x/2}Sn_{1-x}Te$, $Ag_{x/2}In_{x/2}Sn_{1-x}Te$, and $Bi_{x/2}In_{x/2}Sn_{1-x}Te$ samples. In all cases, the carrier mobility at room temperature decreases as the doping fraction increases due to the enhanced ionization impurity scattering, and there are only minor differences between the three-types of dopants which can be ascribed to the fact that the convergence of valence band (separate pockets of Fermi surface with the same energy) introduces the large density-of-states effective mass without explicitly reducing the carrier mobility. [3]

The electrical conductivity (σ) as a function of temperature for the $Mg_{x/2}In_{x/2}Sn_{1-x}Te$, $Ag_{x/2}In_{x/2}Sn_{1-x}Te$, and $Bi_{x/2}In_{x/2}Sn_{1-x}Te$ samples are presented in Figure 4a-c, respectively. It clearly shows that the electrical conductivity of all the samples decreases steadily with increasing temperature up to 873 K, which is typical metallic conduction due to the high hole densities in these samples. With increasing doping concentration, the room temperature σ values drastically decrease for all samples, which should be ascribed to the notable reduction in their carrier mobility, as shown in the inset in Figure 3f. A comparison of the temperature-dependent electrical conductivity for pristine and doped samples with 3% doping concentration is shown in Figure 4d. With identical doping fractions, the Bi&In co-doped samples have the lowest electrical conductivities due to the noticeable reduction in the carrier mobility and carrier concentration, and the Mg&In and Ag&In co-doped samples have intermediate values between the Bi&In co-doped and pristine samples arising from the increase of the carrier concentration (Figure 3f). Specifically, the room-temperature electrical conductivity of SnTe is ~63.9 × 10^4 S m^{-1}, and it decreases to ~35.9, 28.9, and 13.2 × 10^4 S m^{-1} for $Mg_{0.015}In_{0.015}Sn_{0.97}Te$, $Ag_{0.015}In_{0.015}Sn_{0.97}Te$, and $Bi_{0.015}In_{0.015}Sn_{0.97}Te$, respectively.

Because of the increased Seebeck coefficients due to the synergistic effects of the resonant level, valence band convergence, and/or the carrier concentration optimization, the power factors of all the doped samples are dramatically enhanced over a broad temperature range compared with pristine SnTe, as shown in Figure 5a-c. Figure 5d presents the comparison of their power factors at the identical doping fraction (x = 0.03) with previously reported values. Obviously, the co-doping of Mg and In results in a higher improvement of the electrical transport properties, and leads to a higher power factor compared to the cases of doping with Ag&In and Bi&In. In addition, previously reported In-[21] and Mg-doped,[19] In&Cd&CdS-,[17] Cd&CdS-,[20] Bi&HgTe-,[26] and Bi&SrTe-alloyed[25] samples are also compared. These previous works demonstrate that In contributes to the enhancement of the power factor at low temperature, and Mg contributes to the power factor at high temperature. In our case, the power factor is improved over the entire temperature range, leading to noticeably high average electrical transport properties for SnTe.

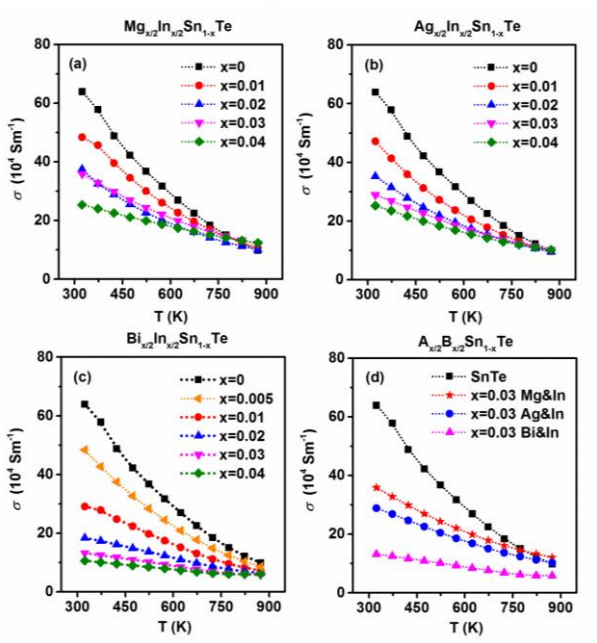

Figure 4. Electrical conductivity as a function of temperature for (a) $Mg_{x/2}In_{x/2}Sn_{1-x}Te$; (b) $Ag_{x/2}In_{x/2}Sn_{1-x}Te$; (c) $Bi_{x/2}In_{x/2}Sn_{1-x}Te$. A comparison of temperature dependence of electrical conductivity for pristine and doped samples with 3% doping concentration is presented in (d).

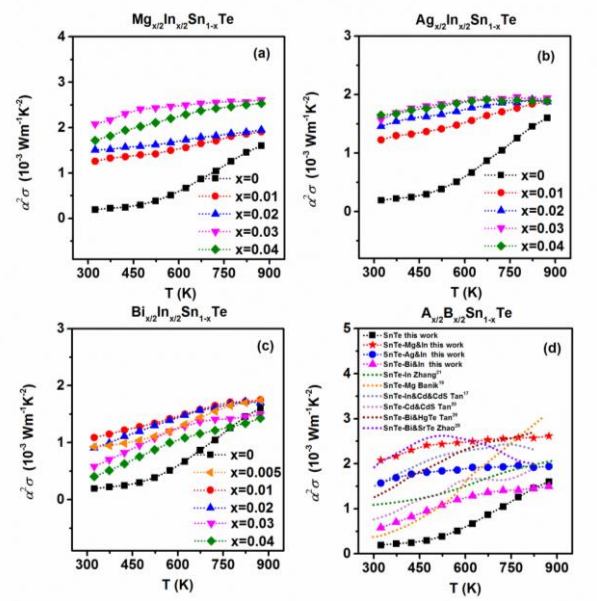

Figure 5. Power factor as a function of temperature for (a) $Mg_{x/2}In_{x/2}Sn_{1-x}Te$; (b) $Ag_{x/2}In_{x/2}Sn_{1-x}Te$; (c) $Bi_{x/2}In_{x/2}Sn_{1-x}Te$. A comparison of temperature dependence of power factors for pristine and doped samples with 3% doping concentration is presented in (d). Previously reported In-doped,[21] Mg-doped,[19] In&Cd&CdS-alloyed,[17] Cd&CdS-alloyed,[20] Bi&HgTe-alloyed,[26] and Bi&SrTe-alloyed [28] samples are also presented.

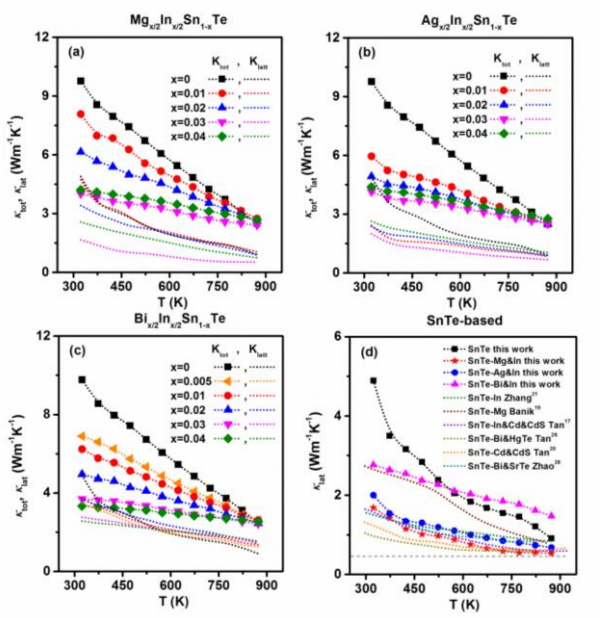

Figure 6. Total thermal conductivity and lattice thermal conductivity as a function of temperature for (a) $Mg_{x/2}In_{x/2}Sn_{1-x}Te$; (b) $Ag_{x/2}In_{x/2}Sn_{1-x}Te$; (c) $Bi_{x/2}In_{x/2}Sn_{1-x}Te$. Comparison of temperature dependence of the lattice thermal conductivity for pristine and Mg&In, Ag&In and Bi&In co-doped samples with 3% doping concentration, with those of previously reported In-doped,[21] Mg-doped,[19] Bi&HgTe-alloyed,[26] In&Cd&CdS-alloyed,[17] Cd&CdS-alloyed,[20] and Bi&SrTe-alloyed[28] samples.

Specifically, the average power factor of pristine SnTe is ~0.73 × 10^{-3} W m^{-1} K^{-2} from 300 to 873 K, it increases to ~1.38 × 10^{-3} W m^{-1} K^{-2} and ~1.51 × 10^{-3} W m^{-1} K^{-2} for Mg-and In-doped samples, respectively, and finally reaches ~2.43 × 10^{-3} W m^{-1} K^{-2} after combining Mg and In co-dopants ($Mg_{0.015}In_{0.015}Sn_{0.97}Te$). Moreover, this average power factor for $Mg_{0.015}In_{0.015}Sn_{0.97}Te$ is also higher than those reported values (~2.0 - 2.3 × 10^{-3} W m^{-1} K^{-2}) for In&Cd&CdS-,[17] Bi&HgTe-,[26] and Bi&SrTe-alloyed[28] samples.

Figure 6a-c shows the total thermal conductivity (κ_{tot}) and lattice thermal conductivity (κ_{lat}) as functions of temperature for $Mg_{x/2}In_{x/2}Sn_{1-x}Te$, $Ag_{x/2}In_{x/2}Sn_{1-x}Te$ and $Bi_{x/2}In_{x/2}Sn_{1-x}Te$, respectively. The κ_{tot} exhibits decreasing trend as the doping concentration increases for all three-types of dopants. Typically, the total thermal conductivity of pristine SnTe is ~2.50 - 9.76 W m^{-1} K^{-1} over the temperature range of 323 - 873 K, which dramatically reduces to ~2.41 - 4.15 W m^{-1} K^{-1} after doping 3% fraction of Mg&In, Ag&In and Bi&In. The reduction of their κ_{tot} for Mg&In and Ag&In doped samples is mainly ascribed to the decreased lattice thermal conductivity, while for the Bi&In doped samples, it is mainly caused by the decrease in the carrier concentration (Figure 3f). Unlike the regular decrease of κ_{tot}, however, the temperature dependence of κ_{lat} is irregular and independent of doping concentration or dopant types. Moreover, the κ_{lat} values are almost half of the κ_{tot} values for all the samples, which indicate the dominance of electron-phonon interactions for SnTe materials.

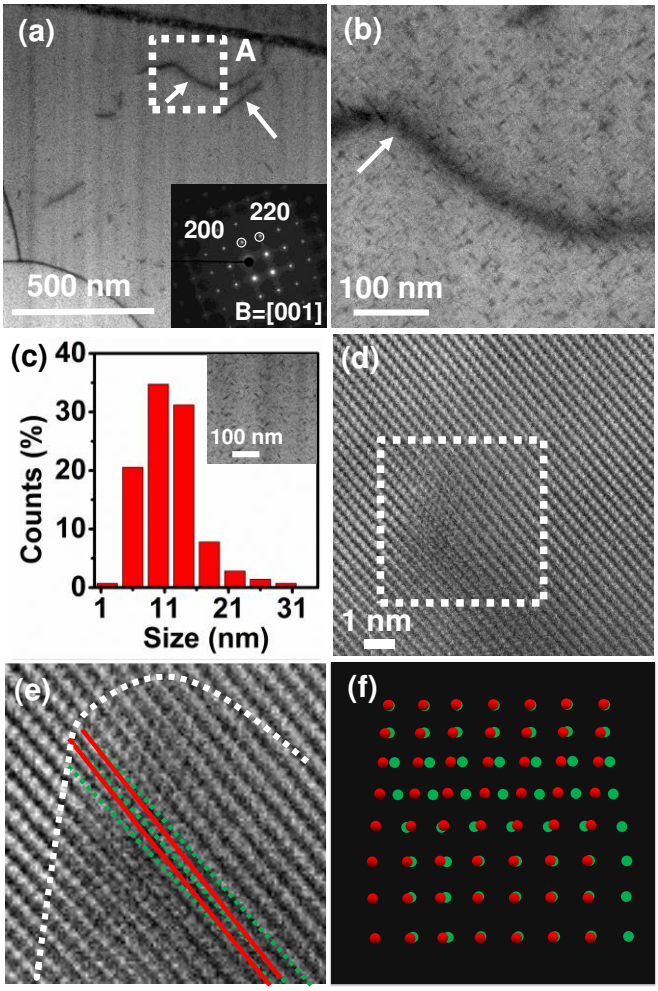

Figure 7. Electron microscope images of the $Mg_{0.015}In_{0.015}Sn_{0.97}Te$ specimen. (a) Low-magnification image of the specimen along the [0 0 1] zone axis, showing large misfit dislocations (white arrows). The inset is the corresponding SAED pattern; (b) Enlarged view of the boxed region in (a), presenting numerous nanoscale elongated dislocations; (c) Histogram of the elongated dislocation size. The inset is the corresponding area used to count the dislocation sizes. (d) HRTEM image of a typical nanoscale elongated dislocation; (e) IFFT images of the boxed region in (d), showing a typical screw dislocation. A schematic illustration of the screw dislocations is shown in (f).

It is worth noting that the lattice thermal conductivity of 3% Mg&In doped samples at 873 K is ~0.54 W m^{-1} K^{-1}, which is very close to its theoretical minimum thermal conductivity, κ_{min} (~ 0.5 W m^{-1} K^{-1}), for SnTe-based materials.[36] This value is also lower than the reported values (0.58 - 0.6 W m^{-1} K^{-1}) for Bi&HgTe-,[26] In&Cd&CdS-,[17] and Cd&CdS-alloyed[20] SnTe samples, as shown in Figure 6d.

To understand the origin of the ultralow lattice thermal conductivity, the microstructure and chemical composition of the $Mg_{0.015}In_{0.015}Sn_{0.97}Te$ sample was investigated by TEM, STEM, and EDS, as shown in Figure 7a-f. Figure 7a shows a low-magnification image along the [0 0 1] orientation with some big misfit dislocations.

These big misfit dislocations are random in length, around 100 - 500 nm. The inset of Figure 7a is the selected area electron diffraction (SAED) pattern of the corresponding area, showing

perfect single cubic SnTe phase. Figure 7b shows an enlarged view of the boxed region in Figure 7a, presenting a high density of nanoscale elongated dislocations with random orientations. The size of the elongated dislocations along the length direction is around 6 - 14 nm (Figure 7c). Figure 8e shows the high resolution transmission electron microscope (HRTEM) image of a typical nanoscale elongated dislocation, which identified by the inverse fast Fourier transform (IFFT) image (Figure 7e), indicating the existence of the screw dislocation. Schematic illustration of a typical screw dislocation is shown in Figure 7f. Other typical screw dislocations and elements distribution are displayed in the Supporting Information Figures S11-S12.

The above high-density elongated screw dislocations with random orientations can provide intensive scattering for phonons along different directions. Moreover, the size of nanoscale dislocations plays a significant role in the propagation pathways of medium wavelength phonons and thus in achieving effective nanoscale phonon scattering.[34] In addition, the introduction of point defects by co-dopants (Mg&In, Ag&In and Bi&In) and grain boundaries by sintering also act as atomic scale and microscale barriers to scatter short and long wavelength phonons, respectively. Thus, with the benefits of this multi-scale scattering, ultralow lattice thermal conductivity (~0.54 W m^{-1} K^{-1}) was achieved in the $Mg_{0.015}In_{0.015}Sn_{0.97}Te$ sample.

The temperature dependence of *ZT* values of $Mg_{x/2}In_{x/2}Sn_{1-x}Te$, $Ag_{x/2}In_{x/2}Sn_{1-x}Te$, and $Bi_{x/2}In_{x/2}Sn_{1-x}Te$ are shown in Figures 8a-c, respectively. In all cases, the *ZT* values are obviously enhanced over the entire temperature range from 323 to 873 K and are strongly dependent on the dopant type and dopant concentration. With the benefits of the higher power factor and the lower lattice thermal conductivity, a high *ZT* ~ 1 was achieved in $Mg_{0.015}In_{0.015}Sn_{0.97}Te$ at 873 K, being 80% higher than that of pristine SnTe. In addition, the average *ZT* over a wide temperature range from 323 to 873 K is improved considerably from ~0.14 for pristine SnTe to ~0.51 for $Mg_{0.015}In_{0.015}Sn_{0.97}Te$ sample (Figure 8d).

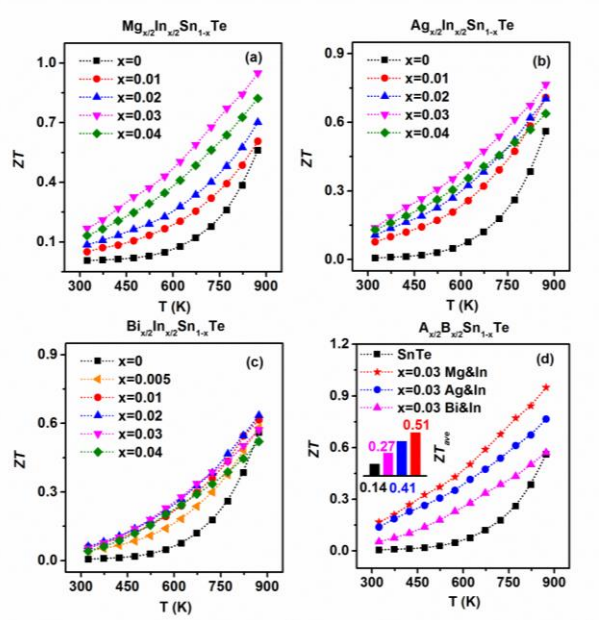

Figure 8. *ZT* as a function of temperature for (a) $Mg_{x/2}In_{x/2}Sn_{1-x}Te$; (b) $Ag_{x/2}In_{x/2}Sn_{1-x}Te$; (c) $Bi_{x/2}In_{x/2}Sn_{1}.xTe$. Comparison of the temperature dependence of *ZT* for pristine and doped samples with 3% doping concentration (d). The inset in (d) is the corresponding average *ZT* over the temperature range from 323 to 873 K.

Conclusion

In summary, the temperature-dependent evolution of Σ band contribution to the Seebeck coefficient of SnTe is revealed *in situ* by neutron and synchrotron powder diffraction over a wide temperature range. The results present that high effective mass of carriers are created in Σ valence band arising from the thermal excitation of holes from the L to Σ band above 493 K. These "heavy" holes contribute to the electrical transport, and significantly enhance the Seebeck coefficient at high temperature. In addition, the coexistence of resonant levels (due to In dopant), band convergence (due to Mg and Ag dopants), and/or the carrier concentration optimization (due to Mg, Ag, and Bi dopants) has synergistically led to broad temperature range. Moreover, the atomic scale point defects (due to In and Mg co-doping), the nanoscale elongated screw dislocations with random directions, and the microscale grain boundaries caused by the sintering efficiently scatter a wide spectrum of heat-carrying phonons, leading to a significant reduction of the lattice thermal conductivity. With the benefit of these factors, a high *ZT* of ~1 at 873 K was achieved for $Mg_{0.015}In_{0.015}Sn_{0.97}Te$ sample. These results suggest that SnTe-based materials could be an important lead-free thermoelectric candidate for power generation, and provide insights for synergistically engineering multiband thermoelectric materials with high performance.

Acknowledgements

Z. Li acknowledges support from the Australian Research Council (ARC) through the Discovery Project DP130102699. S. Dou is grateful for support from the ARC through the Linkage Project LP120200289. The authors are grateful for the support from the Institute for Superconducting and Electronic Materials (ISEM), the Electron Microscopy Centre of the University of Wollongong, the Australian Nuclear Science and Technology Organization, Australian Synchrotron, Jiangsu Provincial Key Laboratory of Radiation Medicine and Protection, and the Priority Academic Program Development Fund of Jiangsu Higher Education Institutions (PAPD). The JEOL JEM-ARM 200F transmission electron microscope was funded by the ARC Grant LE120100104. The authors thank Dr. Tania Silver for critical reading of this manuscript, thank Dr. Qinfen Gu and Dr. Maxim Avdeev for their assistance of SPD and NPD experiments.

References

1 T. Zhu, Y. Liu, C. Fu, J. P. Heremans, J. G. Snyder and X. Zhao, *Adv. Mater.*, 2017, **29**, 1605884

2 S. I. Kim, K. H. Lee, H. A. Mun, H. S. Kim, S. W. Hwang, J. W. Roh, D. J. Yang, W. H. Shin, X. S. Li, Y. H. Lee, G. J. Snyder and S. W. Kim, *Science*, 2015, **348**, 109-114.

3 Y. Pei, X. Shi, A. LaLonde, H. Wang, L. Chen and G. J. Snyder, *Nature*, 2011, **473**, 66-69.

4 L.-D. Zhao, G. Tan, S. Hao, J. He, Y. Pei, H. Chi, H. Wang, S. Gong, H. Xu, V. P. Dravid, C. Uher, G. J. Snyder, C. Wolverton and M. G. Kanatzidis, *Science*, 2016, **351**, 141-144.

5 C. Han, Q. Sun, Z. Li and S. X. Dou, *Adv. Energy Mater.*, 2016, **6**, 1600498.

6 L. Zhang, J. Wang, Q. Sun, P. Qin, Z. Cheng, Z. Ge, Z. Li and S. Dou, *Adv. Energy Mater.*, 2017, DOI: 10.1002/aenm.201700573.

7 J. P. Heremans, V. Jovovic, E. S. Toberer, A. Saramat, K. Kurosaki, A. Charoenphakdee, S. Yamanaka and G. J. Snyder, *Science*, 2008, **321**, 554-557.

8 Q. Zhang, H. Wang, W. Liu, H. Wang, B. Yu, Q. Zhang, Z. Tian, G. Ni, S. Lee and K. Esfarjani, *Energy Environ. Sci.*, 2012, **5**, 5246-5251.

9 J. P. Heremans, B. Wiendlocha and A. M. Chamoire, *Energy Environ. Sci.*, 2012, **5**, 5510-5530.

10 L. Zhao, H. Wu, S. Hao, C.-I. Wu, X. Zhou, K. Biswas, J. He, T. P. Hogan, C. Uher and C. Wolverton, *Energy Environ. Sci.*, 2013, **6**, 3346-3355.

11 L.-D. Zhao, S. Hao, S.-H. Lo, C.-I. Wu, X. Zhou, Y. Lee, H. Li, K. Biswas, T. P. Hogan and C. Uher, *J. Am. Chem. Soc.*, 2013, **135**, 7364-7370.

12 K. Biswas, J. He, Q. Zhang, G. Wang, C. Uher, V. P. Dravid and M. G. Kanatzidis, *Nat. Chem.*, 2011, **3**, 160-166.

13 K. Biswas, J. He, G. Wang, S.-H. Lo, C. Uher, V. P. Dravid and M. G. Kanatzidis, *Energy Environ. Sci.*, 2011, **4**, 4675-4684.

14 Y. Lee, S.-H. Lo, J. Androulakis, C.-I. Wu, L.-D. Zhao, D.-Y. Chung, T. P. Hogan, V. P. Dravid and M. G. Kanatzidis, *J. Am. Chem. Soc.*, 2013, **135**, 5152-5160.

15 K. Biswas, J. He, I. D. Blum, C.-I. Wu, T. P. Hogan, D. N. Seidman, V. P. Dravid and M. G. Kanatzidis, *Nature*, 2012, **489**, 414-418.

16 G. Tan, W. G. Zeier, F. Shi, P. Wang, G. J. Snyder, V. P. Dravid and M. G. Kanatzidis, *Chem. Mater.*, 2015, **27**, 7801-7811.

17 G. Tan, F. Shi, S. Hao, H. Chi, L.-D. Zhao, C. Uher, C. Wolverton, V. P. Dravid and M. G. Kanatzidis, *J. Am. Chem. Soc.*, 2015, **137**, 5100-5112.

18 J. He, X. Tan, J. Xu, G.-Q. Liu, H. Shao, Y. Fu, X. Wang, Z. Liu, J. Xu, H. Jiang and J. Jiang, *J. Mater. Chem. A*, 2015, **3**, 19974-19979.

19 A. Banik, U. S. Shenoy, S. Anand, U. V. Waghmare and K. Biswas, *Chem. Mater.*, 2015, **27**, 581-587.

20 G. Tan, L.-D. Zhao, F. Shi, J. W. Doak, S.-H. Lo, H. Sun, C. Wolverton, V. P. Dravid, C. Uher and M. G. Kanatzidis, *J. Am. Chem. Soc.*, 2014, **136**, 7006-7017.

21 Q. Zhang, B. Liao, Y. Lan, K. Lukas, W. Liu, K. Esfarjani, C. Opeil, D. Broido, G. Chen and Z. Ren, *PNAS*, 2013, **110**, 13261-13266.

22 L. Rogers, *J. Phys. D: Appl. Phys.*, 1968, **1**, 845-852.

23 J. Kafalas, R. Brebrick and A. Strauss, *Appl. Phys. Lett.*, 1964, **4**, 93-94.

24 R. Brebrick and A. Strauss, *Phys. Rev.*, 1963, **131**, 104-110.

25 A. Banik, U. S. Shenoy, S. Saha, U. V. Waghmare and K. Biswas, *J. Am. Chem. Soc.*, 2016, **138**, 13068-13075.

26 G. Tan, F. Shi, J. W. Doak, H. Sun, L.-D. Zhao, P. Wang, C. Uher, C. Wolverton, V. P. Dravid and M. G. Kanatzidis, *Energy Environ. Sci.*, 2015, **8**, 267-277.

27 L. Zhang, J. Wang, Z. Cheng, Q. Sun, Z. Li and S. Dou, *J. Mater. Chem. A*, 2016, **4**, 7936-7942.

28 L.-D. Zhao, X. Zhang, H. Wu, G. Tan, Y. Pei, Y. Xiao, C. Chang, D. Wu, H. Chi and L. Zheng, *J. Am. Chem. Soc.*, 2016, **138**, 2366-2373.

29 V. P. Vedeneev, S. P. Krivoruchko and E. P. Sabo, *Semiconductors*, 1998, **32**, 241-244.

30 C. Han, Q. Sun, Z. X. Cheng, J. L. Wang, Z. Li, G. Q. Lu and S. X. Dou, *J. Am. Chem. Soc.*, 2014, **136**, 17626-17633.

31 H.-S. Kim, Z. M. Gibbs, Y. Tang, H. Wang and G. J. Snyder, *APL Mater.*, 2015, **3**, 041506.

32 J. Zhao, C. Malliakas, D. Bugaris, N. Appathurai, V. Karlapati, D. Chung, M. Kanatzidis and U. Chatterjee, *arXiv* 2014, **1404**, 1807v1803

33 M. Cutler, J. Leavy and R. Fitzpatrick, *Phys. Rev.*, 1964, **133**, A1143.

34 L.-D. Zhao, V. P. Dravid and M. G. Kanatzidis, *Energy Environ. Sci.*, 2014, **7**, 251-268.

35 C. M. Jaworski, V. Kulbachinskii and J. P. Heremans, *Phys. Rev. B*, 2009, **80**, 233201.

36 D. G. Cahill, S. K. Watson and R. O. Pohl, *Phys. Rev. B*, 1992, **46**, 6131-6140.